A numerical study of the seasonal variability of Arabian Sea high-salinity water

T. G. Prasad[1] and M. Ikeda

Division of Ocean and Atmospheric Sciences, Graduate School of Environmental Earth Science, Hokkaido University, Sapporo, Japan

[1] Using a level 2 three-dimensional turbulent closure model, the physical processes affecting the upper-ocean salinity budget in the Arabian Sea have been studied with particular focus on the seasonal variability of the Arabian Sea High-Salinity Water (ASHSW). The volume integrated salt budget terms for four subdomains in the Arabian Sea (south of 10.5°N, north of 10.5°N, east of 62.5°E, and west of 62.5°E) shows a clear balance between the horizontal advection and evaporative freshwater loss in the annual mean. The horizontal advection dominates the seasonal cycle in salinity. The seasonal balance is clear, when the terms of the salt budget are integrated between 10.5°N and 2.5°N and east of 62.5°E. In these subdomains the two major episodes of horizontal advection during winter and summer are both associated with the seasonal reversal of the Arabian Sea circulation. Model estimation of the upper-ocean salinity budget terms integrated between the surface and 100 m for the winter and summer monsoons agree with a qualitative description of the ASHSW variability. After formation in the northern Arabian Sea during the winter monsoon, the ASHSW spreads predominantly southward along the eastern boundary during the summer monsoon. Advection causes salinity to increase by $1.0 \text{ kg m}^{-2} \text{ day}^{-1}$ along these regions. At this time, the poleward advection of low-salinity water from the south (and upwelling regions) by the Somali current causes the salinity along the western Arabian Sea to decrease by $0.6 \text{ kg m}^{-2} \text{ day}^{-1}$. During the winter monsoon, westward advection of the fresher Bay of Bengal water by the North Equatorial current (NEC) causes a salinity decrease by $\sim 1.0 \text{ kg m}^{-2} \text{ day}^{-1}$ in the region south of 10.5°N. The combined effect of precipitation and evaporation tends to increase the salinity in the Arabian Sea, and horizontal advection is found to be important for maintaining the observed seasonal cycle.   *INDEX TERMS:* 4283 Oceanography: General: Water masses; 4255 Oceanography: General: Numerical modeling; 4572 Oceanography: Physical: Upper ocean processes; 4512 Oceanography: Physical: Currents; *KEYWORDS:* Arabian Sea, ASHSW, salt budget, horizontal advection, water masses, freshwater flux

1. Introduction

[2] In the northern Arabian Sea, enhanced evaporative cooling driven by dry air (low humidity) from the north during the winter monsoon is known to be responsible for the convective formation of the Arabian Sea High-Salinity Water (ASHSW) [*Prasanna Kumar and Prasad*, 1996, 1999; *Prasad and Ikeda*, 2002; *Prasad*, 1997, 2001]. The core of the ASHSW, generally found in the upper 100 m (after seasonal subduction as noted by *Han* [1999]) is subjected to large spatiotemporal variability (Figure 1).

[3] The zonally directed Indian Monsoon current (IMC) (Figure 2) in summer and the NEC during winter constitute two important links between the Bay of Bengal and Arabian Sea. The NEC carries fresher water into the Arabian Sea; IMC carries saltier ASHSW into the Bay of Bengal [*Vinayachandran et al.*, 1999; *Han and McCreary*, 2001]. Using a $4\frac{1}{2}$ layer model, *Han and McCreary* [2001] studied the effects of salinity on the dynamics and thermodynamics of the Indian Ocean by introducing different forcing fields that include precipitation minus evaporation (P-E), river input, Indonesian throughflow, and the intrusion of high-salinity Persian Gulf Water (PGW) and Red Sea Water (RSW). They concluded that the salinity distribution can be simulated well provided all of the above forcing fields are included. Their model, however, cannot resolve the fine vertical structure of salinity owing to its limited number of layers; *Han and McCreary* [2001] therefore gave a qualitative discussion of the salinity distribution in the Indian Ocean. *Esenkov* [2000] investigated the salt budget in the Arabian Sea using the Miami Isopycnal Coordinate Ocean Model (MICOM). He argued that only cross-equatorial

---

[1]Now at Department of Oceanography, Naval Postgraduate School, Monterey, California, USA.
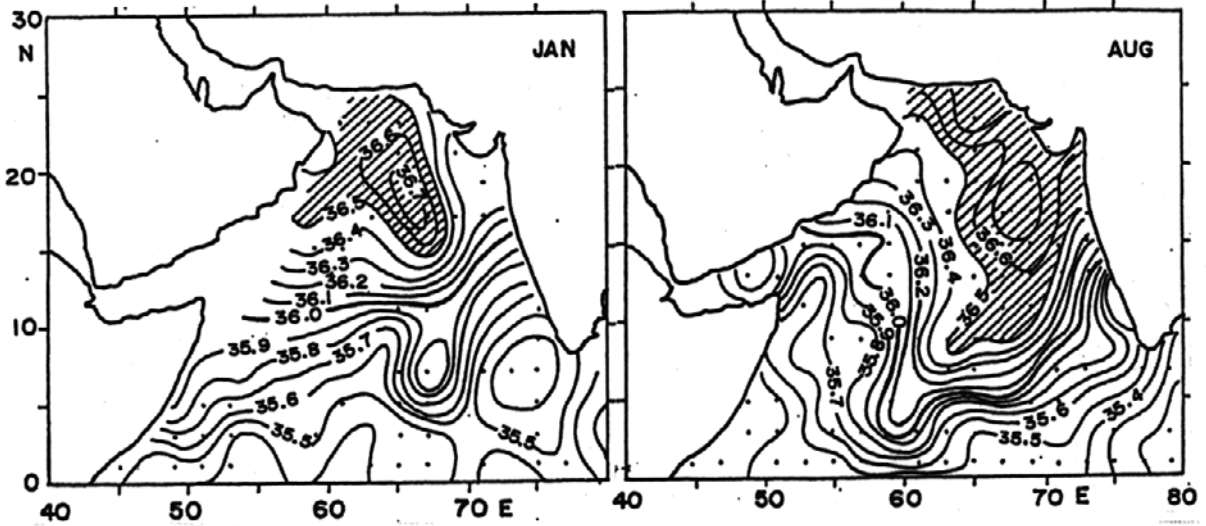
Figure 1. Monthly mean distributions of the salinity of the core of ASHSW for January and August after *Prasanna Kumar and Prasad* [1999]. Hatched regions show the position of the core as defined by salinity >36.5 psu.

transport of low-salinity water in the upper 400 m is important to the salinity budget in the Arabian Sea.

[4] *Prasad and Ikeda* [2002] examined the winter evolution of the ASHSW in a one-dimensional turbulent closure model, neglecting advective and horizontal mixing fields. Although the one-dimensional model did reproduce the observed characteristics of the ASHSW formation, significant differences between the model and observation [*Prasanna Kumar and Prasad*, 1999] were noted in those regions where seasonally reversing wind forces a seasonally reversing surface circulation. The one-dimensional model was also found to be unrealistic in those areas where surface forcing drove Ekman divergence, particularly along the coasts of Somalia, Arabia, and Oman during the summer monsoon. It is thus clear that variations in sea surface salinity can result from several processes (P-E + runoff, horizontal advection, vertical advection induced by the wind stress curl and lateral mixing), suggesting that three-dimensional processes may be of importance in determining the seasonal variability of the ASHSW. The specific processes affecting the upper-ocean salinity (ASHSW) in the Arabian Sea remain to be elucidated. It is this issue we address here.

[5] In this study we use a high vertical resolution model [*Prasad and Ikeda*, 2002] consisting of 100 levels in the upper 200 m (2 m) to simulate the fluxes of momentum, heat, and salt below the mixed layer. Our approach differs from previous modeling efforts in this region which principally employed layered models with generally greater horizontal resolution but limited vertical resolution. The vertical mixing scheme [*Mellor and Yamada*, 1982] employed here is superior to the traditional bulk mixed layer model of *Kraus and Turner* [1967] used in the earlier layer models. The surface features are also better resolved in the turbulent closure model. A model with a fine vertical resolution is capable of resolving a deep mixed layer in summer and winter, which is a useful character to simulate

SST and air-sea heat flux appropriately. The detailed vertical information in the model is used to estimate the ASHSW core properties, that is defined as a local subsurface salinity maximum in the upper 200 m. The rest of the paper is outlined as follows. A brief description of the model equations and forcing fields are presented in section 2. Seasonal variability of the model-derived sea surface temperature (SST), mixed layer depth (MLD), fresh water flux (P-E), and salinity are given in section 3. Then the model fields are used to estimate the salt budget terms in the upper 100 m (sections 4 and 5). A discussion and summary is given in section 6.
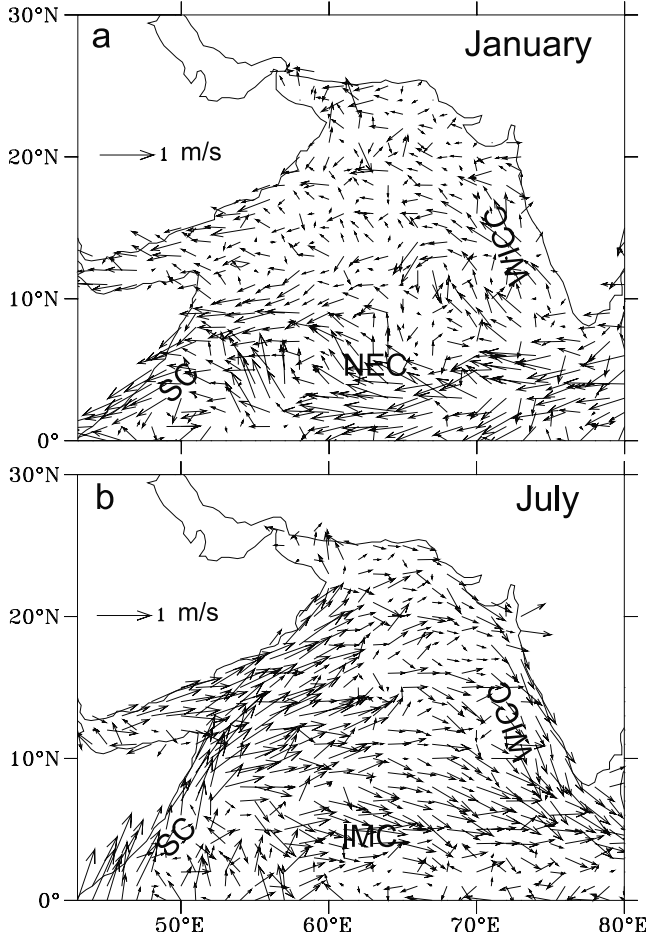
2. Model Equations

[6] The level 2 second-order closure model is based on the assumption that shear and buoyancy production locally balances viscous dissipation [*Mellor and Durbin*, 1975; *Ikeda*, 1986]. The time-dependent, level 2, second-order, 3-D turbulent closure model used here differs from our previous paper [*Prasad and Ikeda*, 2002] in that advective and horizontal mixing terms are included in the temperature and salinity equations:

$$\frac{\partial U}{\partial t} - fV = \frac{\partial}{\partial z}\left(lqS_m\frac{\partial U}{\partial z}\right) \tag{1}$$

$$\frac{\partial V}{\partial t} + fU = \frac{\partial}{\partial z}\left(lqS_m\frac{\partial V}{\partial z}\right) \tag{2}$$

$$\frac{\partial T}{\partial t} + \mathbf{u}\cdot\nabla T + w\frac{\partial T}{\partial z} = \frac{\partial}{\partial z}\left(lqS_h\frac{\partial T}{\partial z}\right) + \mu\nabla^2 T \tag{3}$$

$$\frac{\partial S}{\partial t} + \mathbf{u}\cdot\nabla S + w\frac{\partial S}{\partial z} = \frac{\partial}{\partial z}\left(lqS_h\frac{\partial S}{\partial z}\right) + \mu\nabla^2 S \tag{4}$$

Figure 2. Surface currents (m s^{-1}) determined from the ship-drift climatology of *Mariano et al.* [1995] for January and July representing winter and summer monsoon periods. Major currents are indicated: SC, Somali current; NEC, north equatorial current; WICC, west India coastal current [*Shetye et al.*, 1991]; IMC, Indian monsoon current.

[7] A detailed derivation of the model equations is presented by *Prasad and Ikeda* [2002] and thus is not repeated here. The term μ is the horizontal mixing coefficient for T and S (10^3 m^2 s^{-1}). We decompose the horizontal velocity into geostrophic components and wind-driven ageostrophic components (i.e. **u** = u_g + U, **v** = v_g + V). Equations (1) and (2) were solved for the wind-driven ageostrophic components. Since our focus here is to investigate the seasonal variability of salinity not to predict the current fields, we adopted geostrophic components derived from the observed seasonally varying climatological density field (not dependent on model-derived density field). The geostrophic currents are computed as follows. A new climatology for temperature and salinity was prepared based on Expendable Bathythermograph (XBT), Conductivity-Temperature-Depth (CTD), and Bottle profiles [*Prasad et al.*, 2001] extracted from *Levitus and Boyer*'s [1994] climatology. From this climatology we calculated monthly mean geostrophic currents relative to 400 dbar (since the maximum depth of the XBT profile is limited to 450 m). The resulting velocity components were then multiplied by a factor of two adjustment to dynamic

height relative to a deeper reference level. This factor appears to be a reasonable choice because direct current observations at ~8–9°N during January 1998 show a current band with ~10 cm s^{-1} reaching to almost 1000 m [*Schott and Fischer*, 2000] indicating that a reference level of 1500 m seems to be the best choice. For example, the basin averaged surface dynamic heights calculated from *Levitus and Boyer*'s [1994] climatology for January relative to 400, 1000, and 1500 dbar is 96, 157, and 192 dyn cm, respectively. Here the variability of 0/400 dbar correlates with 0/1000 dbar (0/1500 dbar) with a factor of 1.6 (2.0).

[8] Thus the velocity components used to compute temperature and salinity advection (equations (3) and (4)) are sum of the geostrophic and ageostrophic currents in a linear model. However, the geostrophic currents manifest nonlinear effects on temperature and salinity, which satisfy nonlinear equations including advection terms and contains various effects such as monsoon.

[9] The vertical velocity (w) is calculated following *Lee et al.* [2000]

$$w = \frac{1}{f\rho_o}\left(\nabla \times \overline{\tau} + \frac{\beta}{f}\tau^x\right),$$

where the divergence of the Ekman transport yields two terms: the curl of the wind stress and a term related to the latitudinal variation in Ekman transport (β is the gradient in the planetary vorticity f, and τ^x is the eastward component of the wind stress $\overline{\tau}$). The second term is particularly important in near-equatorial regions.

[10] The model is applied to the Arabian Sea in the domain north of 1.5°N and west of 79.5°E on a horizontal 1° × 1° grid and has 100 vertical levels with 2 m intervals (summarized in Table 1). The model is integrated forward in time with a time step of 40 s.

2.1. Boundary Conditions

[11] The surface boundary conditions at the free surface (z = 0) are specified as in the case of 1-D model:

$$\rho_o lqS_m\left(\frac{\partial U}{\partial z}, \frac{\partial V}{\partial z}\right) = (\tau_x, \tau_y)$$

$$\rho_o C_p lqS_h\frac{\partial T}{\partial z} = Q_o$$

$$\rho_o lqS_h\frac{\partial S}{\partial z} = S(E - P).$$

The model's southern and eastern boundaries were open, and an upstream temperature and salinity condition was applied using the monthly mean values from *Levitus and Boyer* [1994]. All other boundaries are closed (no normal flow of heat/salt flux) and river input in the Arabian Sea was neglected as its effect on salinity variations is negligible. The lower boundary was fixed at 200 m where an upstream boundary condition was applied as described above.

2.2. Surface Forcing

[12] The model forcing function was calculated from climatological fields of monthly mean solar radiation (Q_{sw}), scalar wind, vector wind (**V**), air temperature (T_a), relative humidity (RH), and cloudiness (C) taken from the

Table 1. Parameters for Three-Dimensional Arabian Sea Simulations

Parameter	Notation	Value
Model domain		$43.5-80.5°E$, $1.5-29.5°N$
Horizontal resolution	$(\Delta X, \Delta Y)$	$1° \times 1°$
Vertical resolution	ΔZ	2 m
Bottom level		200 m
Time Step	ΔT	40 Sec.
Mixing coefficient	μ	$10^3 \, m^2 s^{-1}$
Drag coefficient for wind stress (τ_x, τ_y)	C_D	2.0×10^{-3}
Coefficient for sensible heat flux Q_S	C_S	1.1×10^{-3}
Coefficient for latent heat flux Q_L	C_L	$1.2 \times 10^{-3} + 3.3 \times 10^{-4}(T_s - T_a)$ $\|T_s - T_a\| \leq 3°C$ $1 \times 10^{-3} \leq C_L \leq 2 \times 10^{-3}$

Comprehensive Oceanographic and Atmospheric Data Set (COADS) [*Rao et al.*, 1989]. These data, provided on a 2° × 2° grid for each month, were bilinearly interpolated in space onto the model grid. The sensible and latent heat fluxes and longwave radiation were estimated from these fields using model SST rather than observed SST [see *Prasad and Ikeda*, 2002]. Precipitation data was provided by *Legates and Willmott* [1990].

[13] To model the observed increase of C_L with air-sea temperature difference [*Bunker*, 1976], C_L was assumed to vary linearly with ($T_s - T_a$) for $\|T_s - T_a\| \leq 3°C$. Beyond this range, C_L was fixed at its maximum or minimum values of 2×10^{-3} and 1×10^{-3} [*McCreary et al.*, 1993; *McCreary and Kundu*, 1989]. The wind stress was calculated from

$$\tau = \rho_a C_D |\mathbf{V}|\mathbf{V},$$

where $\rho_a = 1.175 \, Kg \, m^{-3}$ is the density of air and $C_D = 2.0 \times 10^{-3}$. Such a high value of C_D is recommended for use with monthly mean winds to account for the effects of high-frequency wind exerts on vertical mixing [*Hastenrath and Lamb*, 1979; *McCreary and Kundu*, 1989].

[14] The model integration was initiated in April, during the transition period between the summer and winter monsoons when the wind is weak with the model initialized with observations of temperature and salinity taken from *Levitus and Boyer* [1994] and started from rest. The model was integrated forward in time for a period of 14 months by which time the seasonality is reproduced. The advective timescale for a water parcel to travel from the ASHSW formation region to the southern boundary is ~10 months with a constant velocity of 10 cm s^{-1}. Observations indicated a 5 month time period (June–October) for ASHSW to reach the equatorial region from the formation region [*Prasanna Kumar and Prasad*, 1999] that qualifies our period of integration. Because our aim here is to simulate the observed seasonal variability of the ASHSW, we have not integrated the model to a steady state. Furthermore, in the following salt budget analysis we consider salinity in the upper 100 m that has undergone a complete seasonal cycle. The model results were written every 2 days with a vertical resolution of 4 m, and the results shown here are from the last 12 months of the simulation.

3. Results

[15] We begin by examining the evolution of the upper-ocean thermal fields, sea surface temperature (SST), and mixed layer depth (MLD) that are pertinent to characteristics of the ASHSW. For brevity we will present figures of the fields for 2 months, January and August, representing the winter and summer monsoons. Freshwater flux and salinity are discussed together and compared with the observations.

3.1. SST and MLD

[16] In Figures 3 and 4 we present monthly mean SST and MLD from the model and corresponding observations, respectively. The MLD is taken as the depth at which the temperature is less than 1°C from the SST [*Rao et al.*, 1989]. Generally, the seasonal cycle of the model-derived SST and MLD fields agree well with observations, with an error of <0.5°C in SST. In the Arabian Sea, MLD and SST are characterized by semiannual variations with maximum MLD (cool SST) during midwinter and midsummer and relatively shallow MLD (warm SST) during spring and fall.

[17] From March through May, increased stratification due to solar heating under light winds bring the mixed layer depth to a minimum (10–40 m) while SST rises. In June, MLD begins to deepen (60 m) in the central Arabian Sea as the winds pick up. MLD attains a maximum value in
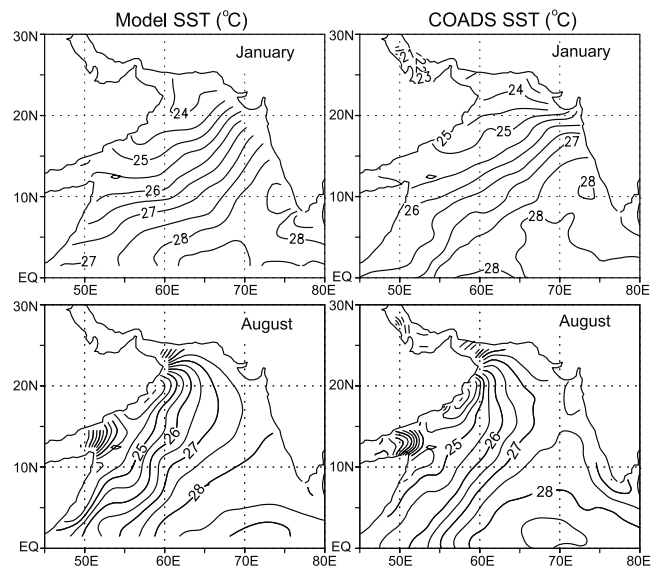
Figure 3. Monthly mean sea surface temperature (SST) from the model solution for January and August (left panel) and from COADS climatology (right panel). Contour interval is 0.5°C.
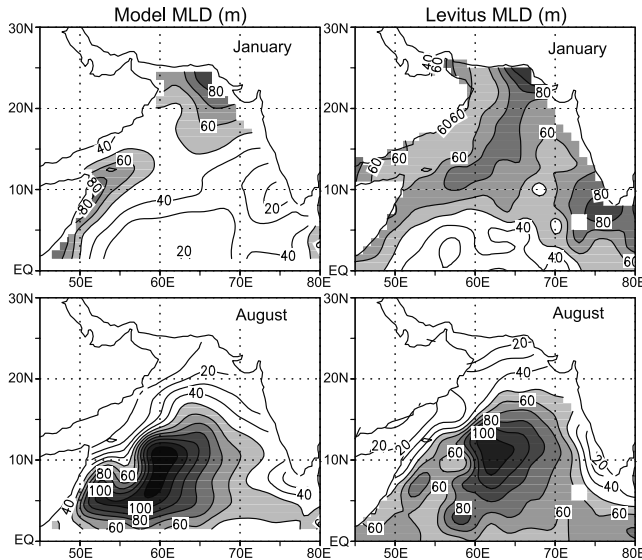
Figure 4. Monthly mean mixed layer depth (MLD) field for January and August. Model MLD (left panel) and from *Levitus and Boyer* [1994] climatology (right panel). MLD is defined as the depth at which the temperature is <1°C from the SST. Contour interval is 10 m; shading is provided for values greater than 50 m.

August (110 m) in the central Arabian Sea that persists until the end of September, in agreement with the observations. There are two mechanisms acting together to deepen the MLD: wind-driven vertical mixing and Ekman convergence. Of these, the wind-driven mixing has the greatest impact. MLD shoals along the coasts of Somalia, Arabia, and Oman owing to Ekman divergence driven by positive wind stress curl. As a result, cool SST appears along these regions from mid-May to September. Offshore advection of coastally upwelled waters is also evident. During October the MLD becomes shallow owing to weak winds.

[18] From November through February the MLD deepens (60 m) and SST steadily cools (<25°C) in the northern Arabian Sea. During this period the northern Arabian Sea experiences a net heat loss (-40 W m^{-2}) from the ocean (figures not presented) owing to elevated latent heat flux driven by the dry air emanating from the north. Thus negative buoyancy driven convective mixing is the mechanism for deep MLD and cool SST in the northern Arabian Sea. The significant difference in MLD in the southeastern Arabian Sea is associated with an anticyclonic eddy, the Lakshadweep High [*Bruce et al.*, 1994], which drives a deep MLD (80 m) during the winter monsoon.

3.2. Seasonal Cycle of the ASHSW

[19] In this section we provide a qualitative description of the time-varying ASHSW core salinity distribution driven by freshwater flux (P-E) (Figure 5) and monsoonal changes in the Arabian Sea circulation. This is elucidated quantitatively further in section 4. In the following descriptions the subsurface salinity maxima in the upper 200 m are used to examine the seasonal variability of the ASHSW core properties. A direct comparison of model-derived ASHSW core properties is possible with the climatological ASHSW core properties of *Prasanna Kumar and Prasad* [1999]. The

position of ASHSW core, which lies at the surface in the northern Arabian Sea and below the mixed layer (100 m) in the equatorial region generally agrees with the observations. Note that the salinity contour of 36.0 psu in bold face has been chosen to demarcate the spatial extent within which the ASHSW is prominent. This contour also best represents the seasonal migration of the ASHSW core owing to the seasonally reversing monsoon currents. In the following discussion we begin with a description of the winter monsoon, the period of ASHSW formation in the north and freshening in the south followed by the summer monsoon features, the period during which the ASHSW flows south from its northern formation region.

[20] The model-generated bimonthly ASHSW core distributions depicted in Figure 6 reveal large spatial and temporal variability consistent with the observations. In the Arabian Sea the winter monsoon is characterized by moderate winds from the northeast from November through February. During December a salinity front separating saltier ASHSW to the west and fresher Bay of Bengal water to the east appears in the southeastern Arabian Sea. Zonal advection (as can be seen from the successive monthly maps) displaces this front westward bringing fresher water into the Arabian Sea. By April, the entire region south of 10°N freshens as indicated by the northward migration of the 36.0 psu contour. From November through February the salinity north of 10°N increases progressively, reaching more than 36.6 psu in the northern Arabian Sea. Elevated evaporative cooling (Figure 5) resulting from the influence of the dry and relatively cool northeast monsoon winds produce the ASHSW.

[21] At the equator a strong eastward flow (equatorial jet) [*Wyrtki*, 1973] develops in November in response to the westerly winds. The part of the ASHSW that reaches the equator (between 60–65°E) during October–November (see 36.0 psu contour) may move into the Bay of Bengal
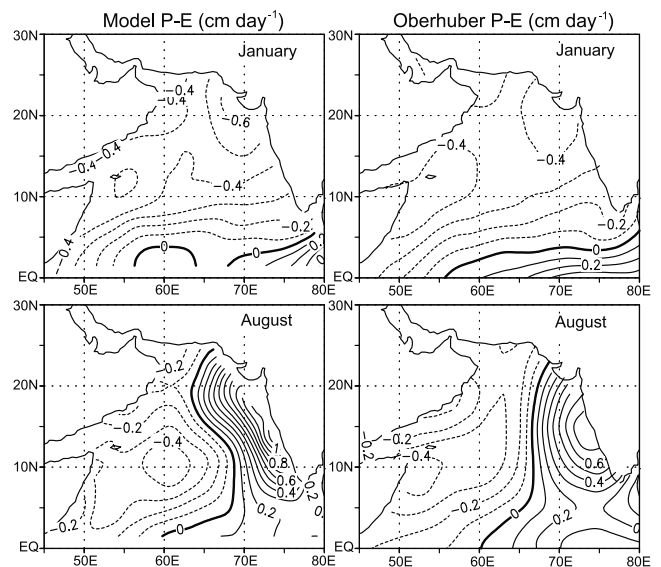
Figure 5. Monthly mean precipitation-evaporation (P-E, cm day^{-1}) from the model (left panel) and from the *Oberhuber* [1988] climatology (right panel). Dashed lines indicate net freshwater loss. Contour interval is 0.1 cm day^{-1} with the zero contour emphasized.
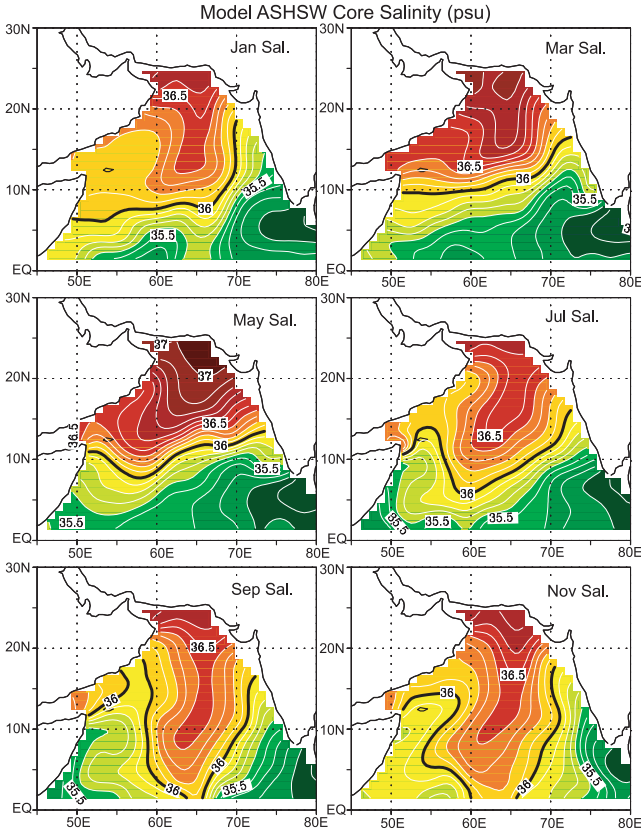
Figure 6. Bimonthly mean ASHSW core salinity from the model. The core is defined as the local salinity maximum in the upper 200 m. Contour interval is 0.1 psu, and shading is provided at 0.2 psu intervals. Contour 36.0 psu is emphasized to indicate the seasonal migration associated with the seasonal circulation.

by the equatorial jet as suggested by *Han and McCreary* [2001]. At this time an accompanying low-salinity water mass that appears in the equatorial region precludes the possibility that low salinity in this region is advected from the east (because saltier ASHSW occurs in the east). The northward advection of low-salinity water from the south may be a possible source (see map for January in Figure 6).

[22] The summer monsoon period spans mid-May to September in the Arabian Sea. From June through September the saltier ASHSW in the northern Arabian Sea spreads southward within the central Arabian Sea as evidenced by the 36.0 psu contour. As a result, the ASHSW core salinity in the equatorial region increases ~0.5 psu from 35.5 (winter) to 36.0 psu (September). Effects of freshwater gain (due to relatively intense rain) along the west coast of India (P-E > 0, Figure 5) on ASHSW variations are not apparent. Along the coasts of Somalia, Arabia, and Oman one would expect a salinity increase due to the excess freshwater loss (P-E < 0) in this period, but the salinity actually decreases. For example, salinity along the Omani coast reduces from 36.4 (April) to 36.0 psu during summer.

3.3. Model-Data Comparison

[23] Our model-derived ASHSW core pattern agrees reasonably well with the climatology [*Levitus and Boyer*,

1994; *Prasanna Kumar and Prasad*, 1999]. Generally, model core salinity in the northern Arabian Sea 36.5–36.8 psu is 0.1–0.3 psu higher than from the *Levitus and Boyer* [1994] climatology. However, salinities >36.8 psu were reported along a section close to the shelf (section A–D of *Lee et al.* [2000]) and at the core of the ASHSW (>36.7 psu) [*Prasanna Kumar and Prasad*, 1999]. *Morrison* [1997] and *Morrison et al.* [1998] provided a description of the temporal and spatial variability in temperature and salinity properties along the cross-basin sections in the northern Arabian Sea. Their description agrees with the model-derived salinity seasonal evolution. A comparison of the time series salinity fields sampled at 61.5°E, 15.5°N [*Rudnick et al.*, 1997] and model salinity demonstrates that the presence of high salinity during April–May at the moored site is due to the southward spreading of ASHSW. The salinity drops sharply in June in both the model and observations, indicating the presence of fresher water from the southern upwelling regions. Surface layer freshening was also noted in alongshore and across-basin sections during June–July [*Lee et al.*, 2000]. This water may have had its origin near the Somali coast and was subsequently advected to the moored array site by the strong Somali current during the summer monsoon. Thus the upper ocean salinity variability simulated by the model agrees reasonably well with the limited view of the observations.
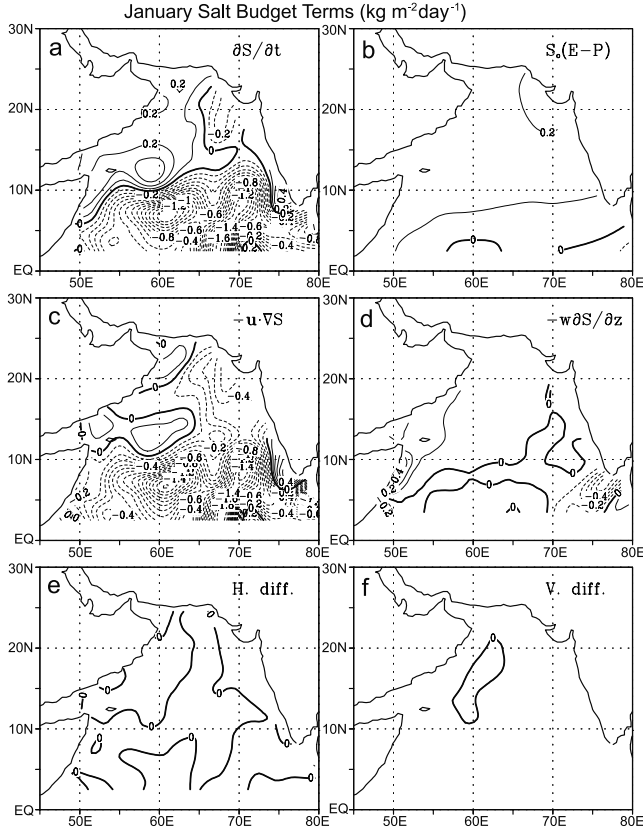
[24] There are, however, some discrepancies between the model and observed salinity fields. First, the strong across-shelf salinity gradient along the west coast of India during October–November seen in the *Prasanna Kumar and Prasad* [1999] climatology is less evident in the model ASHSW core salinity, probably caused by the poor representation of the coastal currents. Second, southward spreading of the ASHSW during summer occurs farther west in the model than that in the observation. This may result from the fact that the Ekman drift dominates the geostrophy at the surface along the western side. In support of this idea the salinity at 50 m shows a pattern that agrees better with the observations (figure not presented).

4. Upper-Ocean Salt Budget

[25] What might be the processes affecting the upper-ocean salt balance in the Arabian Sea? The model fields provide a four-dimensional (x, y, z, t) data set from which one can determine the relative importance of various terms in the salt budget. In the following temporal evolution of salt budget analysis we take $h = 100$ m lower boundary. This selection provides maximum information of the mixed layer (because maximum MLD is around 100 m during both seasons, Figure 4). Vertically integrating the salt tendency equation (4) from a fixed depth h (= 100 m) to the sea surface, the following expression is obtained,

$$\int_{-h}^{o} \frac{\partial S}{\partial t} dz = -\int_{-h}^{o} \left(\mathbf{u} \cdot \nabla S + w \frac{\partial S}{\partial z} \right) dz - S_o(P-E) + F_S|_{-h}$$

$$+ \mu \int_{-h}^{o} \nabla^2 S dz, \tag{5}$$

January Salt Budget Terms (kg m^{-2}day^{-1})

Figure 7. Monthly mean salt budget terms in the upper 100 m for January in kg m^{-2} day^{-1}. The salt-budget terms include (a) temporal rate of salinity change ($\partial S/\partial t$) due to (b) freshwater flux (S_o(E-P)), (c) horizontal advection ($\mathbf{u} \cdot \nabla S$), (d) vertical advection ($w\partial S/\partial z$), (e) horizontal diffusion and (f) vertical diffusion. The contour interval is 0.1 kg m^{-2} day^{-1}.

where F_S is the vertical turbulent salt flux calculated at 100 m,

$$F_S = lqS_h\frac{\partial S}{\partial z}.$$

[26] Thus the local change in the vertically integrated salinity can be due to the effect of the surface freshwater flux, horizontal advection, vertical advection, and vertical and horizontal diffusive terms. In the following salt budget analysis a constant value of $\rho = 1025$ kg m^{-3} is used to express the integrated salinity in kg m^{-2} day^{-1}.

[27] Monthly mean salt budget terms integrated between 100 m and surface in the Arabian Sea are presented for January (Figure 7) and August (Figure 8) representing two monsoons. Interestingly, a large part of the salinity tendency in the upper 100 m is due to horizontal advective divergence. During January, freshening due to horizontal advection dominates the salinity tendency in the regions south of 10°N and along the west coast of India. During this time the NEC advects fresher Bay of Bengal water into the Arabian Sea, which results in a depth-integrated salinity loss of >1.2 kg m^{-2} day^{-1}. Part of the Bay of Bengal water is subsequently advected poleward by the WICC causing a

0.4 kg m^{-2} day^{-1} reduction of salinity. There is a mild salinity increase (0.2 kg m^{-2} day^{-1}) in the northwestern region primarily due to evaporation. During August the salinity changes are induced by the reversing currents. The southeastward Ekman drift and geostrophic current along the eastern branch of the anticyclonic gyre in the interior Arabian Sea together with the WICC carry salty ASHSW equatorward, increasing the depth-integrated salinity by 1.0 kg m^{-2} day^{-1} in the eastern Arabian Sea. A comparably sized salinity decrease (0.8 kg m^{-2} day^{-1}) occurs in the western Arabian Sea owing to the poleward advection of low-salinity water by the Somali current. Excess evaporation along western Arabian Sea (0.1 kg m^{-2} day^{-1}) locally increases the depth-integrated salinity, while large precipitation in the east freshens the upper layer salinity by 0.2 kg m^{-2} day^{-1}. Effects of upwelling on salinity variations are more apparent along the coasts of Arabia and Oman (-0.2 kg m^{-2} day^{-1}). Downward advection of high-salinity water in the downwelling region (central Arabian Sea) contribute a 0.2 kg m^{-2} day^{-1} salinity increase.

[28] In the following discussion on temporal evolution of the salt-budget terms we divide the Arabian Sea north of 2.5°N into four subdomains with dividing lines at 10.5°N and 62.5°E. This is done to isolate the dominant processes affecting the upper-ocean salinity variability in each of these regions. It may be noted that our salt budget subdomains are overlapped. The salt budget terms integrated over these volumes are presented in the following sections. Thus the time rate of change of volume integrated salinity is the result

August Salt Budget Terms (kg m^{-2}day^{-1})
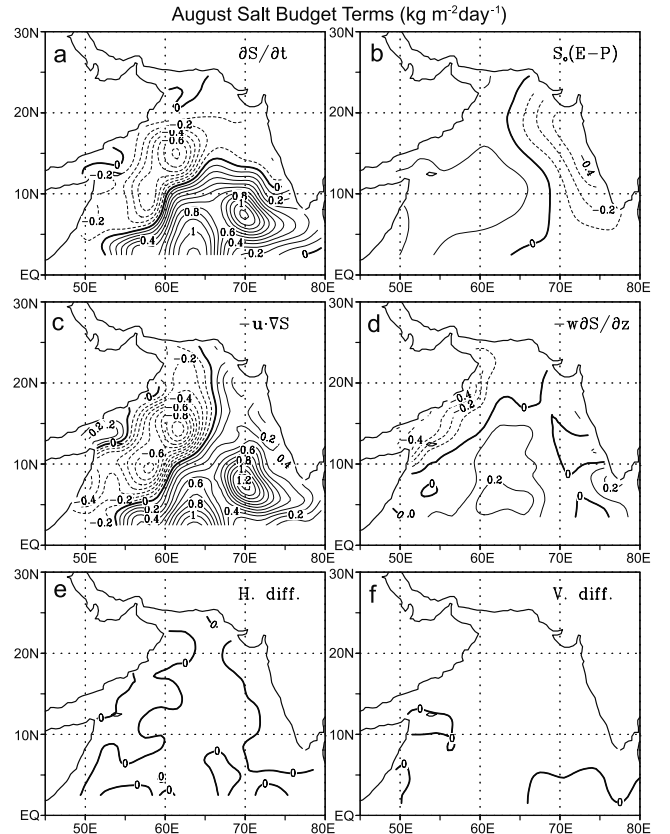
Figure 8. Same as Figure 7 but for August in kg m^{-2} day^{-1}. The contour interval is 0.1 kg m^{-2} day^{-1}.
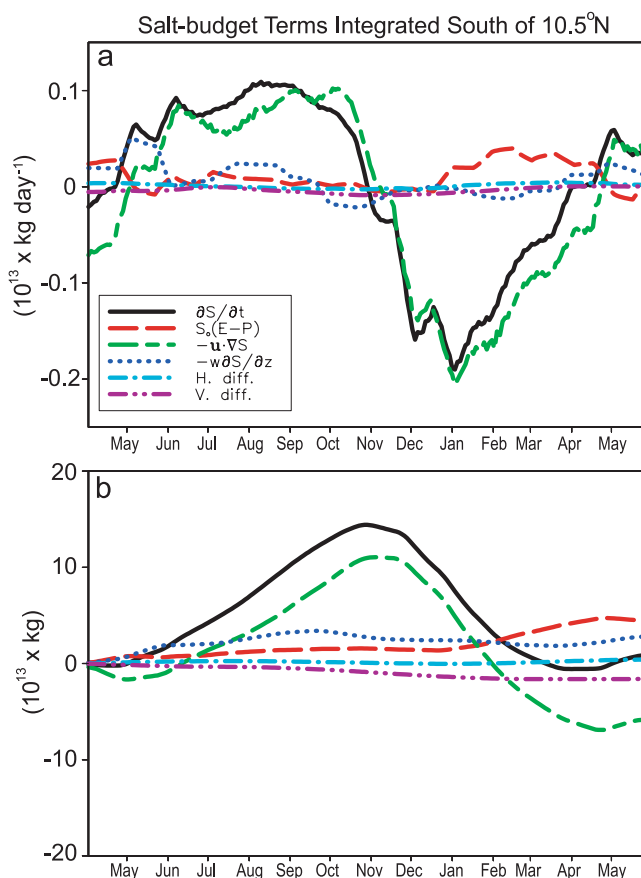
Figure 9. Salt budget terms in the upper 100 m integrated south of 10.5°N in kg day^{-1} (a) and the corresponding cumulative salt budget terms in kg (b). The salt budget terms include temporal rate of salinity change due to freshwater flux (S_o(E-P)), horizontal advection ($\mathbf{u} \cdot \nabla S$), vertical advection (w$\partial S/\partial z$), vertical and horizontal diffusion.

of flux divergences across the horizontal and vertical ocean boundaries of each region and air-sea freshwater exchange.
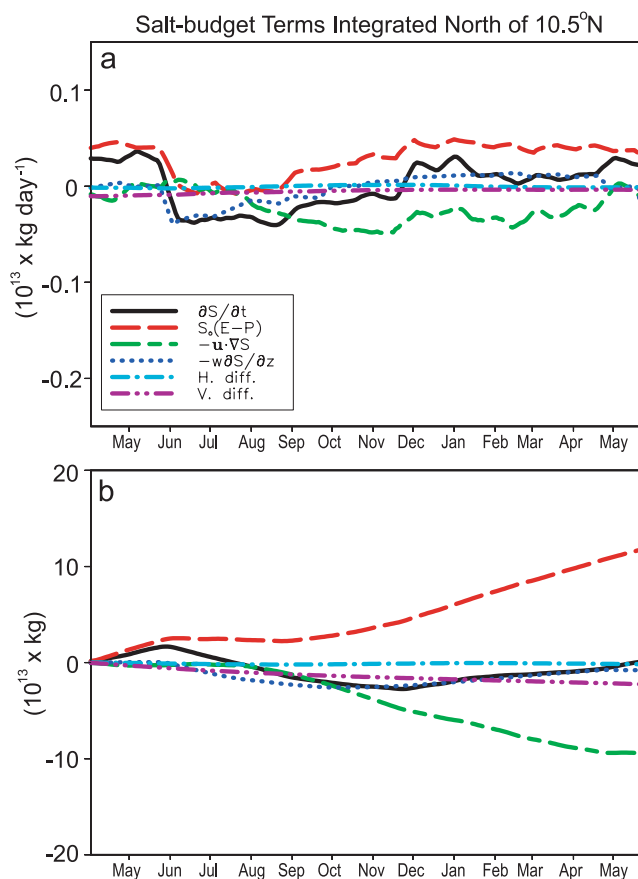
4.1. South of 10.5°N

[29] Figure 9a shows the volume integrated salt budget terms, and Figure 9b shows its cumulative effect. During this time period the seasonal cycle in salinity variability is clearly indicated. The seasonal cycle is dominated by the horizontal advective divergence, and vertical advection and surface flux (E-P) are small in affecting the upper-ocean salinity. The salinity trend ($\partial S/\partial t$) and horizontal advection terms tend to cancel each other. The temporal variation of the volume integrated salinity is of the order of 0.05–0.1 × 10^{13} kg day^{-1} during summer and increases to 0.15 × 10^{13}

Table 2. Salt Imbalance After a Year (April)

Regions	Salt Imbalance, mm
South of 10.5°N	−55
North of 10.5°N	−95
East of 62.5°E	−124
West of 62.5°E	−3
North of 2.5°N	−80

kg day^{-1} during the peak winter (January). The increase in volume-integrated salinity during summer is primarily the result of horizontal advective divergence across the northern boundary of the region. The change in sign of the horizontal advection in November is due to the reversal of the circulation in this region. During winter, westward advection of fresher Bay of Bengal water across the eastern boundary accounts for major salinity decrease with little contribution from the south.

[30] The precipitation-evaporation has a cumulative effect of 5 × 10^{13} kg during a 1 year time period, tending to increase the salinity (Figure 9b). The effect of vertical advection is to increase the volume-integrated salinity. The horizontal advection term plays a major role in balancing the combined effect of evaporative freshwater flux and vertical advection and accounts for a change of −6 × 10^{13} kg. The net effect of horizontal diffusion is negligibly small; vertical diffusion causes a decrease in the salinity (−2 × 10^{13} kg). The salinity imbalance from the model calculated after a year (April) is ∼−0.58 × 10^{13} kg (−55 mm) and is summarized for each regions in Table 2. This error could be due to the fact that model has not reached the steady state, or it could be due to the uncertainty in the forcing fields. Yet the annual cycle is much larger than the mismatch for 1 year period.

4.2. North of 10.5°N

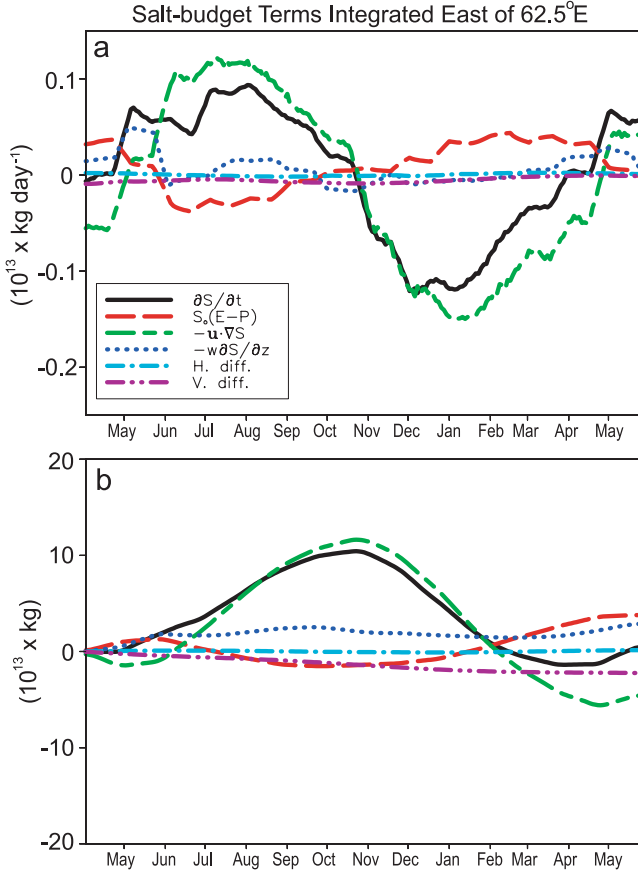[31] The volume-integrated rate of change of salinity north of 10.5°N (Figure 10a) shows a weak seasonal trend (0.03 ×

Figure 10. Same as in Figure 9 but integrated for the region north of 10.5°N.

Salt-budget Terms Integrated East of 62.5°E

Figure 11. Same as in Figure 9 but integrated for the region east of 62.5°E.

10^{13} kg day^{-1}) much smaller than that in the southern region. The vertical advection (Ekman divergence) causes a decrease in the volume-integrated salinity during early summer (-0.03×10^{13} kg day^{-1}). From August the horizontal advection of fresher water from the south tends to decrease the volume-integrated salinity (also see Figures 7 and 8) while loss of freshwater at the surface tends to increase the salinity. The change in sign of the salinity trend term in late November coincides with the ASHSW formation period. As a cumulative result, the horizontal advection accounts for -9×10^{13} kg (reduction of salinity) acting to compensate for salinity increase by 10×10^{13} kg due to air-sea freshwater loss in the northern Arabian Sea and the vertical diffusion (-2×10^{13} kg) balancing the difference out (Figure 10b).

4.3. East of 62.5°E

[32] The seasonal cycle of the volume-integrated salinity trend in this region is dominated by the horizontal advective divergence across the regional boundaries (Figure 11a). Since this region overlaps with the previous two regions, the salt budget terms are comparable in the region south of 10.5°N (see Figure 9). Horizontal advection of fresher water southward across the region during summer causes an increase in volume integrated salinity (0.05×10^{13} kg day^{-1}). A comparable quantity of fresher water (-0.06×10^{13} kg day^{-1}) enters the region during winter primarily across the eastern boundary. Air-sea freshwater gain (loss) at the surface during summer (winter) accounts for a change

of volume-integrated salinity to -0.02×10^{13} kg day^{-1} (0.04×10^{13} kg day^{-1}). The horizontal advection becomes a freshening process in November as a result of westward directed current at the eastern boundary.

[33] As a cumulative result, the net effect of combined precipitation and evaporation is to increase the volume-integrated salinity in the upper 100 m and account for a change of 3×10^{13} kg (Figure 11b). However, horizontal advection brings more fresh water into the region, decreasing the salinity slightly by -5×10^{13} kg. Vertical diffusion and advection terms partially account for this difference, and the imbalance is $\sim -1.4 \times 10^{13}$ kg (-124 mm) over a year period.

4.4. West of 62.5°E

[34] The time rate of change of volume-integrated salinity shows a semiannual variability (Figure 12a). In the annual mean, evaporation is the dominant term in the salinity budget and horizontal advection is the important process influencing salinity variability. Both summer and winter monsoon periods indicate a decrease in the volume-integrated salinity (-0.03×10^{13} kg day^{-1}) due primarily to the horizontal advection (-0.05×10^{13} kg day^{-1}). While summer freshening is a result of poleward flow across the southern boundary, it is the flow across the eastern boundary that decreases the volume integrated salinity during winter. During June–July, vertical advection (upwelling) causes a decrease in the volume-integrated salinity by 0.02×10^{13} kg day^{-1}. The combined precipitation and evaporation has a cumulative

Salt-budget Terms Integrated West of 62.5°E
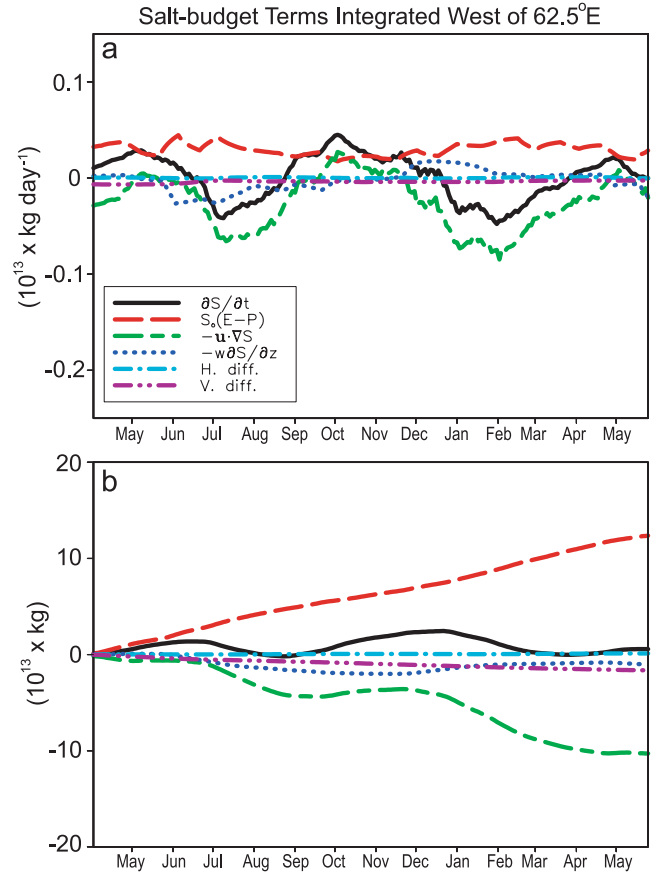
Figure 12. Same as in Figure 9 but integrated for the region west of 62.5°E.
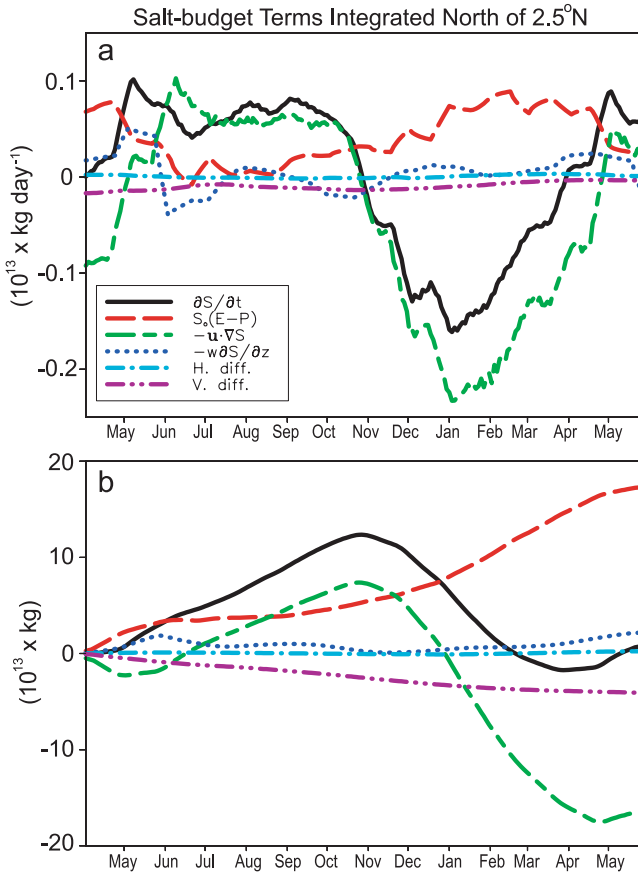
Figure 13. Same as in Figure 9 but integrated for the region north of 2.5°N.

effect of 11×10^{13} kg, tending to increase the volume-integrated salinity (Figure 12b). Compensation of the freshwater loss by the horizontal advection is to decrease the salinity and account for a change of -10×10^{13} kg. The residual is $\sim -0.03 \times 10^{13}$ kg (-3 mm) over this time period.

4.5. North of 2.5°N

[35] The volume-integrated salinity tendency term north of 2.5°N (Figure 13a) in the Arabian Sea is due to the horizontal advective divergence. From May through late

October the horizontal advection causes an increase in salinity to 0.05×10^{13} kg day^{-1}. During this period the surface currents are northward along the western boundary and equatorward along the eastern side. The southward advection of saltier ASHSW in the east overwhelms weak freshening in the west yields a net increase in volume-integrated salinity during summer (0.05×10^{13} kg day^{-1}). During winter the freshwater loss due to excess evaporation tends to increase the volume-integrated salinity, while horizontal advection brings fresher water into the basin, causing a net salinity decrease (-0.1×10^{13} kg day^{-1}). The combined precipitation and evaporation has a cumulative effect of 15×10^{13} kg, tending to increase the salinity and freshening due to horizontal advection account for a change of -17×10^{13} kg balancing this out, thereby maintaining salinity balance in the basin (Figure 13b). After a year, the net imbalance is $\sim -1.7 \times 10^{13}$ kg (-80 mm).

5. Components of Salt Flux

[36] We separated velocity (**V**) and salinity (**S**) fields across the ocean boundaries (1) $\rho \int \langle \mathbf{V} \rangle \langle S \rangle L(z) \, dz$ and (2) $\rho \int \int \mathbf{V}' S' \, dx dz$ as the sum of the baroclinic salinity flux due to the horizontally averaged vertical meridional circulation and horizontal salinity flux due to the large-scale gyre circulation and the smaller-scale eddies. Here, **V** is the horizontal velocity normal to the ocean boundaries, S is salinity along the ocean boundaries, $\langle \mathbf{V} \rangle$ and $\langle S \rangle$ are the corresponding horizontally averaged baroclinic values, $\mathbf{V}'$ and S' are the departures from that average, i.e. $\mathbf{V} = \langle \mathbf{V} \rangle + \mathbf{V}'$, $S = \langle S \rangle + S'$, $L(z)$ is width of the section at each depth, and $\rho = 1025$ kg m^{-3}.

[37] Monthly mean values of the baroclinic and horizontal salinity fluxes across the four ocean boundaries were computed and summarized in Table 3. To satisfy mass conservation, the horizontally averaged flow (equation (1)) must be balanced by the vertical flow across 100 m level. It appears from Table 3 that it is this mode of salinity flux that dominates the salt budgets in the Arabian Sea.

[38] A significant contribution of salt flux in the Arabian Sea occurs across the 79.5°E due to baroclinic salinity flux. The baroclinic contribution of salinity flux is westward during October–April reaching a maximum value of 5.5 $\times 10^{13}$ kg day^{-1} in February. The salinity flux due to the baroclinic component across 2.5°N is northward (except

Table 3. Monthly Mean Values of the Salinity Flux Contribution Across the Four Ocean Boundaries Come From Spatially Averaged Flow on the Ocean Boundaries and Departures From That Average[a]

Months	2.5°N (1) ×10¹³	(2) ×10¹³	10.5°N (1) ×10¹³	(2) ×10¹³	79.5°E (1) ×10¹³	(2) ×10¹³	62.5°E (1) ×10¹³	(2) ×10¹³
January	12.6272	−0.0783	4.5942	−0.0164	−4.1968	0.0016	1.0286	−0.0293
February	6.8921	−0.0487	3.8933	−0.0088	−5.5809	−0.0018	−0.0932	0.0089
March	0.4753	−0.0026	2.9390	0.0014	−4.6684	0.0022	−0.1965	0.0238
April	0.3523	−0.0114	2.3722	−0.0043	−1.3277	0.0055	−0.7115	0.0441
May	2.3125	−0.0399	0.4170	0.0051	2.0940	0.0030	0.4592	0.0259
June	5.6014	−0.0485	−2.0686	0.0045	2.5087	−0.0003	0.8998	0.0319
July	7.6897	−0.0692	−2.5393	−0.0082	2.5596	−0.0001	1.0008	0.0489
August	6.3441	−0.1098	−1.9502	−0.0309	2.1312	0.0003	1.4097	0.0276
September	0.5918	−0.0763	−0.9301	−0.0552	0.9596	0.0002	0.7794	0.0007
October	−1.3012	−0.0430	1.6230	−0.0671	−0.3774	0.0001	−0.0867	−0.0095
November	1.2650	−0.0368	4.2152	−0.0600	−1.4062	0.0052	1.3532	−0.0199
December	11.7280	−0.0827	4.7730	−0.0343	−2.0988	0.0039	1.8485	−0.0471

[a] See section 5 for details. The units of salinity flux components are in $\times 10^{13}$ kg day^{-1}.
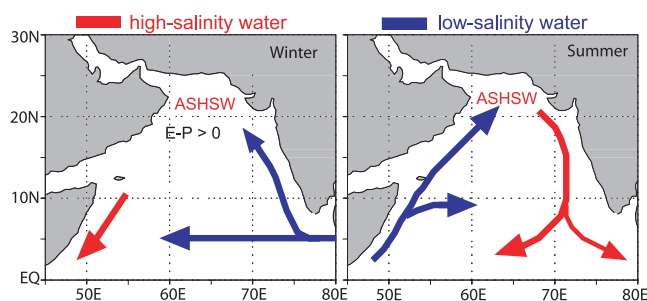
Figure 14. Schematic illustration of the spreading of saltier ASHSW (red arrow) and advection of low-salinity water into the Arabian Sea (blue arrow) during winter and summer monsoons.

during October) reaching a peak value in January (12.5 × 10^{13} kg day^{-1}), and salinity flux contribution from $\mathbf{V'}$ and S' yields a value of 0.05 × 10^{13} kg day^{-1}. The baroclinic salinity flux across 10.5°N is southward during summer (June to September). Similar transport was also noted by *Chereskin et al.* [2002] across 8.5°N based on the World Ocean Circulation Experiment (WOCE) observations.

6. Discussions and Conclusion

[39] Using a second order level 2 three-dimensional turbulent closure model, we studied the seasonal spreading of the ASHSW in the Arabian Sea and identified the physical processes affecting the salinity variability in the upper 100 m. The model-derived sea surface temperature (SST), mixed layer depth (MLD), and freshwater flux (E-P) are in general accord with the observations. The model-derived subsurface salinity maxima associated with the ASHSW core suggests that the seasonal variability of the ASHSW core is strongly dependent on the monsoonal changes of circulation in the Arabian Sea that are in general agreement with the climatological maps of *Prasanna Kumar and Prasad* [1999]. The seasonal variability is more pronounced south of 10°N (~35.5–36.0 psu), whereas salinities are higher in the north during every season (>36.4 psu).

[40] Calculation of salt budget terms integrated in the upper 100 m suggests that the time rate of change of salinity in the Arabian Sea is dominated by the horizontal advective divergence. There are two major episodes of strong horizontal advection and both are associated with the seasonal reversal of the circulation. During summer monsoon the southward advection of saltier ASHSW from the north along the eastern boundary increases the salinity by ~1.0 kg m^{-2} day^{-1}. During winter monsoon the westward advection of fresher Bay of Bengal water by the NEC contributes a freshening of ~1.0–1.3 kg m^{-2} day^{-1} in the region south of 10°N. In the northern Arabian Sea, however, the evaporative freshwater loss (0.1 kg m^{-2} day^{-1}) is the significant contributor to the salinity increase, and horizontal advection (−0.1 kg m^{-2} day^{-1}) plays a major role in balancing this out, thereby maintaining the salinity balance in the upper 100 m. A schematic illustration depicted in Figure 14 shows the spreading of the saltier ASHSW and advection of low-salinity water into the Arabian Sea during winter and summer monsoons. It is worth mentioning that the seasonal spreading of ASHSW

agrees with that of Persian Gulf Water mass (PGW) [*Prasad et al.*, 2001] in the Arabian Sea.

[41] The basin scale salt budget analysis presented here generally agrees with the qualitative description of the salinity variability in the Arabian Sea presented by *Prasanna Kumar and Prasad* [1999] and *Han and McCreary* [2001]. In contrary to the findings of *Esenkov* [2000] our analysis suggests that a significant amount of salt flux across the eastern ocean boundary is important for the salinity budget in the Arabian Sea. However, the cross-equatorial transport of low-salinity water during summer monsoon is important to compensate for high evaporative freshwater loss in the western Arabian Sea. The decomposition of horizontal flow across the ocean boundaries suggests that it is the correlation between the spatially average velocity and spatially average salinity that dominates salt budget in the Arbian Sea.

[42] There are, however, some drawbacks in our model: First, the linear currents used to calculate the advection of temperature and salinity equations, and second, the model was integrated for a period of only 14 months. In our previous endeavor [*Prasad and Ikeda*, 2002] we showed that the formation of ASHSW can be simulated reasonably well in a one-dimensional model. Here we showed that including advection and mixing fields in a simple model could reproduce the basic details of the ASHSW variability. Further progress in accurate simulation of fully resolved vertical structure of salinity and to study the long-term trend in the water mass distribution in the Indian Ocean requires a nonlinear OGCM with an efficient vertical and horizontal (isopycnal) mixing schemes implemented and research in this direction is underway.

References

Bruce, J. G., D. R. Johnson, and J. C. Kindle, Evidence for eddy formation in the eastern Arabian Sea during the northeast monsoon, *J. Geophys. Res.*, 99, 1651–7664, 1994.

Bunker, A. E., Computations of surface energy flux and annual air-sea interaction cycles of the North Atlantic/Indian Ocean, *Mon. Weather Rev.*, 104, 1122–1140, 1976.

Chereskin, T. K., W. D. Wilson, and L. M. Beal, The Ekman temperature and salt fluxes at 8°30′ in the Arabian Sea during the 1995 southwest monsoon, *Deep Sea Res., Part II*, 49, 1211–1230, 2002.

Esenkov, O. E., A numerical study of the dynamics of the somali current system, Ph.D. thesis, 140 pp., Univ. of Miami, Coral Gables, Fla., 2000.

Han, W., Influence of salinity on dynamics, thermodynamics and mixed layer physics in the Indian Ocean, Ph.D. thesis, 147 pp., Nova Southeastern Univ., Dania, Fla., 1999.

Han, W., and J. P. McCreary, Modeling salinity distributions in the Indian Ocean, *J. Geophys. Res.*, 106, 859–877, 2001.

Hastenrath, S., and P. J. Lamb, *Climatic Atlas of the Indian Ocean*, part II, *The Ocean Heat Budget*, 93 pp., Univ. of Wisconsin Press, Madison, Wisc., 1979.

Ikeda, M., A mixed layer beneath melting sea ice in the marginal ice zone using a one-dimensional turbulent closure model, *J. Geophys. Res.*, 91, 5054–5060, 1986.

Kraus, E. B., and J. S. Turner, A one-dimensional model of the seasonal thermocline II: The general theory and its consequences, *Tellus*, 19, 98–106, 1967.

Lee, C. M., B. H. Jones, K. H. Brink, and A. S. Fischer, The upper ocean response to monsoonal forcing in the Arabian Sea: Seasonal and spatial variability, *Deep-Sea Res., Part II*, 47, 1177–1226, 2000.

Legates, D. R., and C. J. Willmott, Mean seasonal and spatial variability in gauge corrected global precipitation, *Int. J. Clim.*, 10, 111–127, 1990.

Levitus, S., and T. P. Boyer, *World Ocean Atlas*, vol. 94, pp. 1–4, NOAA/NESDIS/OCL, Washington, D.C, 1994.

Mariano, A. J., E. H. Ryan, B. D. Perkins, S. Smithers, The Mariano Global Surface Vector Analysis 1.0., *USCG Rep. CG-D-34-95*, 55 pp., 1995.

McCreary, J. P., P. K. Kundu, and R. L. Molinari, A numerical investigation of dynamics, thermodynamics and mixed layer processes in the Indian Ocean, *Prog. Oceanogr.*, *31*, 181–244, 1993.

Mellor, G. L., and P. A. Durbin, The structure and dynamics of the ocean surface mixed layer, *J. Phys. Oceanogr.*, *5*, 718–728, 1975.

Mellor, G. L., and T. Yamada, Development of a turbulent closure model for geophysical fluid problems, *Rev. Geophys.*, *20*, 851–875, 1982.

Morrison, J. M., Inter-monsoonal changes in the T-S properties of the near-surface waters of the northern Arabian Sea, *Geophys. Res. Lett.*, *24*, 2553–2556, 1997.

Morrison, J. M., L. A. Codispoti, S. Gairin, B. Jones, V. Manghnani, and Z. Zheng, Seasonal variations of hydrographic and nutrient fields during the US JGOFS Arabian Sea process study, *Deep Sea Res., Part II*, *45*, 2053–2101, 1998.

Oberhuber, J. M., An atlas based on COADS data set, *Tech. Rep. 15*, 182 pp., Max-Planck Inst. für Meteorol., Hamburg, Germany, 1988.

Prasad, T. G., Annual and seasonal mean buoyancy fluxes for the tropical Indian Ocean, *Current Sci.*, *73*, 667–674, 1997.

Prasad, T. G., Formation and seasonal spreading of water masses in the Arabian Sea based on data analysis and modeling, Ph.D. thesis, 130 pp., Graduate School of Environ. Earth Sci., Hokkaido Univ., Sapporo, Japan, 2001.

Prasad, T. G., and M. Ikeda, The winter-time watermass formation in the northern Arabian Sea: A model study, *J. Phys. Oceanogr.*, *32*, 1028–1040, 2002.

Prasad, T. G., M. Ikeda, and S. Prasanna Kumar, Seasonal spreading of the Persian Gulf Water mass in the Arabian Sea, *J. Geophys. Res.*, *106*, 17,059–17,071, 2001.

Prasanna Kumar, S., and T. G. Prasad, Winter cooling in the northern Arabian Sea, *Current Sci.*, *71*, 834–841, 1996.

Prasanna Kumar, S., and T. G. Prasad, Formation and spreading of Arabian Sea high salinity water mass, *J. Geophys. Res.*, *104*, 1455–1464, 1999.

Rao, R. R., R. L. Molinari, and J. F. Festa, Evolution of the climatological near-surface thermal structure of the tropical Indian Ocean, 1, Description of mean monthly mixed layer depth, sea surface temperature, surface current, and surface meteorological fields, *J. Geophys. Res.*, *94*, 10,801–10,815, 1989.

Rudnick, D. L., R. A. Weller, C. C. Eriksen, T. D. Dickey, J. Marra, and C. Langdon, Moored instruments weather Arabian Sea Monsoons, yield data, *Eos Trans. AGU*, *78*, 120–121, 1997.

Schott, F., and J. Fischer, The winter monsoon circulation of the northern Arabian Sea and Somali Current, *J. Geophys. Res.*, *105*, 6359–6376, 2000.

Shetye, S. R., A. D. Gouveia, S. C. S.Shenoi, G. S. Michael, D. Sunder, A. A. Almeida, and K. Sandanam, The coastal currents off western India during north east monsoon, *Deep-Sea Res., Part I*, *38*, 1517–1529, 1991.

Vinayachandran, P. N., Y. Masumoto, T. Mikawa, and T. Yamagata, Intrusion of the southwest monsoon current into the Bay of Bengal, *J. Geophys. Res.*, *104*, 11,077–11,085, 1999.

Wyrtki, K., An equatorial jet in the Indian Ocean, *Science*, *181*, 262–264, 1973.

_____

M. Ikeda, Division of Ocean and Atmospheric Sciences, Graduate School of Environmental Earth Science, Hokkaido University, N-10, W-5, Sapporo 060 0810, Japan. (mikeda@ees.hokudai.ac.jp)

T. G. Prasad, Department of Oceanography, Naval Postgraduate School, Monterey, CA 93943, USA. (prasad@nps.navy.mil)